LaneCPP: Continuous 3D Lane Detection using Physical Priors

Maximilian Pittner[1,2], Joel Janai[1], Alexandru P. Condurache[1,2]

[1]Bosch Mobility Solutions, Robert Bosch GmbH

[2]Institute of Signal Processing, University of Lübeck

{Maximilian.Pittner, Joel.Janai, AlexandruPaul.Condurache}@de.bosch.com

Abstract

Monocular 3D lane detection has become a fundamental problem in the context of autonomous driving, which comprises the tasks of finding the road surface and locating lane markings. One major challenge lies in a flexible but robust line representation capable of modeling complex lane structures, while still avoiding unpredictable behavior. While previous methods rely on fully data-driven approaches, we instead introduce a novel approach LaneCPP that uses a continuous 3D lane detection model leveraging physical prior knowledge about the lane structure and road geometry. While our sophisticated lane model is capable of modeling complex road structures, it also shows robust behavior since physical constraints are incorporated by means of a regularization scheme that can be analytically applied to our parametric representation. Moreover, we incorporate prior knowledge about the road geometry into the 3D feature space by modeling geometry-aware spatial features, guiding the network to learn an internal road surface representation. In our experiments, we show the benefits of our contributions and prove the meaningfulness of using priors to make 3D lane detection more robust. The results show that LaneCPP achieves state-of-the-art performance in terms of F-Score and geometric errors.

1. Introduction

Robust and precise lane detection systems build one of the most essential components in the perception stack of autonomous vehicles. While some approaches utilize LiDAR sensors or multi-sensor setups, the application of monocular cameras has become more popular due to their lower cost and the high-resolution visual representation that provides valuable information to detect lane markings.

In the past, lane detection was mainly treated as a 2D detection task. Deep learning based methods achieved good results by treating the problem as a segmentation task in pixel space [7, 11, 16, 26, 29, 33, 53], used to classify and regress lanes using anchor-based [19, 41] representations,

or as key-points on a grid structure [13, 15, 34, 45]. However, due to the lack of depth information, these 2D representations fail to model lane markings and road geometry in 3D space, which forms an important prerequisite for later functionalities like trajectory planning. Consequently, approaches for monocular 3D lane detection were introduced, which adapted lane representations for the 3D domain by modeling vertical anchors [6, 9] or local segments on a grid [4] in a Birds-Eye-View (BEV) oriented 3D-frame.

A crucial topic for the application of lane detection algorithms in autonomous systems is safety, which requires predictable and robust behavior in any traffic situation. One risk of learning-based methods is the tendency to show unpredictable behavior in cases of rarely observed scenarios. Since obtaining large amounts of data with high-quality annotations is cumbersome and expensive, publicly available 3D datasets are limited in size and accuracy. Hence, they do not reflect the variability of real-world scenarios sufficiently. This makes learning-based models prone to overfitting, and eventually, diminishes predictability.

One common way to deal with such problems is the integration of prior knowledge. Physics provides us a profound understanding of the 3D world, allowing us to make valid assumptions about the lane structure and road surface geometry. Therefore, we introduce physically motivated priors into the lane detection objective to cope with the limited data problem and achieve robust and predictable behavior.

There are certain geometric properties that should generally hold for detected lane lines. For instance, we know that most lines progress parallel to each other, reside on a smooth surface and should not exceed certain thresholds in terms of curvature and slope. However, integrating such assumptions into prevailing discrete representations is not straight forward as strong simplifications are necessary. In contrast, continuous 3D lane representations directly provide parametric curves using polynomials [1, 23] or more sophisticated B-Splines [32]. These allow for analytical computations on the curve function, which enables the integration of such priors into the lane representation. By modeling these priors explicitly instead of learning them from

data, the model can focus its full capacity on learning richer features for the lane detection task.

We can further use physical knowledge about the road geometry to support the model in learning an internal transformation from image features to 3D space. While methods based on Inverse Perspective Mapping (IPM) [4, 6, 9, 17, 23, 32] make false flat-ground assumptions, learning based transformations [1, 2, 46] completely ignore road properties. In contrast, integrating prior knowledge about the road surface allows us to model 3D features geometry-aware and helps the network to focus on the 3D region of interest.

Thus, we propose a novel 3D lane detection approach named LaneCPP that leverages valuable prior knowledge to achieve accurate and robust perception behavior. It introduces a new sophisticated continuous curve representation, which enables us to incorporate physical priors. In addition, we present a spatial transformation component for learning a physically inspired mapping from 2D image to 3D space providing meaningful spatial features.

Our main contributions can be summarized as follows:
- We propose a novel architecture for 3D lane detection from monocular images using a more sophisticated flexible parametric spline-based lane representation.
- We present a way to incorporate priors about lane structure and geometry into our continuous representation.
- We introduce a new way to use prior knowledge about the road surface geometry for learning spatial features.
- We demonstrate the benefits of our contributions in several ablation studies.
- We show state-of-the-art performance of our model.

2. Related work

Different Lane Representations. An important design choice in deep learning based lane detection is the representation that the network uses to model lane line geometry, which can be categorized as follows: *1) Pixelwise* representations, which formulate lane detection as a segmentation problem, were used mainly in 2D methods [7, 11, 16, 26, 29, 33, 51, 53] and were adopted in 3D by SALAD [50] combining line segmentation with depth-prediction. These representations come with high computational load since a large amount of parameters is required. *2) Grid-based* approaches divide the space into cells and model lanes using local segments [13] or keypoints [15, 34, 45]. 3D-LaneNet+ [4] suggests to use local line-segments and BEV-LaneDet [46] defines key-points on a BEV grid representation. Both depend on the grid resolution and require costly post-processing to obtain lines. *3) Anchor-based* representations [19, 40, 41, 52] model lines as straight anchors with positional offsets at predefined locations. They are widely used in 3D detection approaches including 3D-LaneNet [6] and Gen-LaneNet [9], which use vertical anchors in the top-view, and An-

chor3DLane [12], introducing anchor projection with iterative regression. Similar to grid-based representations, it requires subsequent curve-fitting to obtain smooth lines. *4) Continuous curve* representations [5, 22, 24, 43, 44] instead directly model smooth curves without requiring costly post-processing. While CLGO [23] and CurveFormer [1] use simple polynomials, 3D-SpLineNet [32] proposes B-Splines [3]. Since B-Splines offer local control over curve segments, they are compatible to model complex shapes with low-degree basis functions, while polynomials and Bézier curves show global dependence and thus require higher degrees causing expensive computation. Although 3D-SpLineNet achieves superior detection performance on synthetic data, it unfortunately lacks flexibility as the curve formulation is limited to monotonically progressing lanes, making it hardly applicable to real-world data. To resolve this issue, we propose a more flexible representation based on actual 3D B-Splines. In contrast to discrete grids and anchors, continuous representation even allow us to integrate prior knowledge in an analytical manner.

Geometry Priors. Several approaches suggest to incorporate prior knowledge into learning-based methods, e.g. by integrating invariance into the model architecture [35, 36] or task-specific transformations as for trajectory planning [10, 47, 49]. In the field of lane detection, line parallelism has been formulated as a hard constraint to resolve depth ambiguity and determine camera parameters [27, 48]. Deep declarative networks [8] offer a general framework to incorporate arbitrary properties as constraints, by solving a constrained optimization problem in the forward pass. While such methods are appropriate when hard constraints must be enforced, our goal is rather to guide the network in learning typical geometric lane properties by formulating soft constraints in a regularization objective. Such a regularization only affects training and does not require resolving an optimization problem in the forward pass, and thus, comes without additional computational cost during inference. Following this paradigm, SGNet [24, 40] proposes to penalize the deviation of lateral distance from a constant lane width in the IPM warped top-view, but ignores that the property does not hold for lines deviating from the ground plane. GP [17] presents a parallelism loss that enforces constant distance between nearest neighbors locally, which depends on the number of anchor points. In contrast, our method presents a way to learn parallelism globally and independent of resolutions of discrete lane representations. We propose an elegant way to learn parallelism as well as other geometry priors using analytical formulations of tangents and normals, which are well-defined on our continuous spline representation.

Leveraging 3D Features. An important model component consists in the extraction of 3D features, encoding valuable information to detect lanes along the road surface.
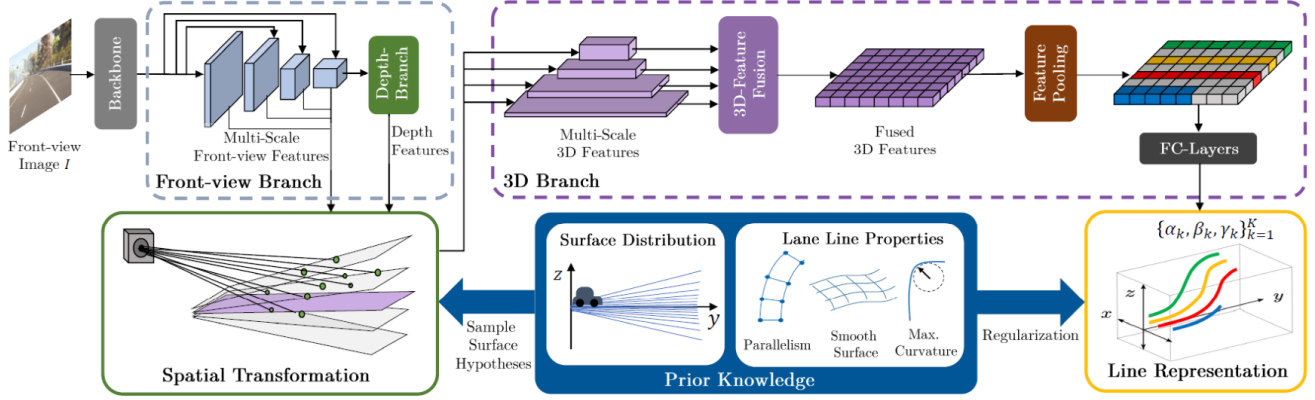
Figure 1. Our approach: First, front-view image I is propagated through the backbone extracting multi-scale feature maps. These are transformed to 3D using our spatial transformation and then fused to obtain a single 3D feature map. Feature pooling is applied to obtain features for each line proposal that are propagated through fully connected layers to obtain the parameters for our line representation. Finally, prior knowledge is exploited to regularize the lane representation and to produce surface hypotheses for the spatial transformation.

While some works predict 3D lanes directly from the front-view, e.g. by utilizing pixel-wise depth estimation [50] or 3D anchor-projection mechanisms [12], prevalent methods employ an intermediate 3D or BEV feature representation with an internal transformation from the front-view to the 3D space. 3D-LaneNet [6] proposes to utilize IPM [25] to project front-view features to a flat road plane due to the spatial correlation between the warped top-view image and 3D lane geometry and was adopted in several other works [4, 9, 17, 23, 32]. However, IPM causes visual distortions in the top-view representation when the flat road assumption is violated. In related fields like BEV semantic segmentation, BEV transformations are learned via Multi-Layer-Perceptrons (MLPs) [18, 28], depth prediction [31, 37, 38] or transformer-based attention mechanisms [20, 30, 39]. In 3D lane detection, PersFormer [2] utilizes attention between front- and top-view, CurveFormer [1] introduces dynamic 3D anchors that model queries as parametric curves and BEV-LaneDet [46] uses MLPs for the spatial transformations. However, these learned transformations do not necessarily provide a 3D feature representation since they are not guided by valuable priors about the road surface geometry, which potentially results in unforeseen behavior for out-of-distribution data. Our approach instead aims for carefully modeling a geometry-aware feature space using a depth classification method inspired by [31] that exploits knowledge about the distribution of the road surface.

3. Methodology

The following section describes our 3D lane detection approach. An overview of the overall architecture is described and illustrated in Fig. 1. The main focus lies on our continuous 3D lane line representation, our regularization mechanism using physical priors and our prior-based spatial trans-
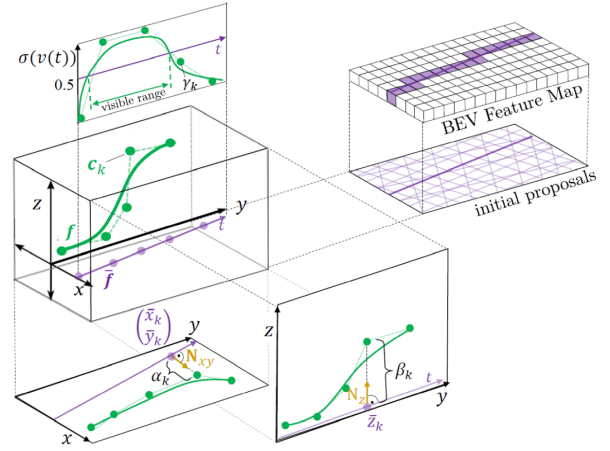

Figure 2. Our 3D lane line representation: For each proposal $\bar{\boldsymbol{f}}$ (purple lines), line geometry is described by 3D B-Splines with control points $\boldsymbol{c}_k$ (green dots). Each control point is determined by the offsets α_k, β_k from the control points of the initial proposal in normal direction (orange vectors). Additionally, visibility $v(t)$ is modeled by splines with 1D control points γ_k.

formation module, which we explain in the following.

3.1. Lane line representation

Inspired by prior work in 3D lane detection [32], we leverage the benefits of continuous representations and employ a parametric model based on B-Splines. However, modeling only lateral (x-) and vertical (z-) components with spline-based functions (as done in previous approaches) is limited to lanes that merely progress along the longitudinal (y-) direction. Instead, we propose the first full 3D lane line representation modeling each component (x, y, z) such that we

obtain

$$\boldsymbol{f}(t) = \begin{pmatrix} x(t) \\ y(t) \\ z(t) \end{pmatrix} = \sum_{k=1}^{K} \boldsymbol{c}_k \cdot B_{k,d}(t) \qquad (1)$$

with curve argument $t \in [0, 1]$ and K control points $\boldsymbol{c}_k = \left(x_k, y_k, z_k \right)^T$. Each control point $\boldsymbol{c}_k$ weights the respective basis function $B_{k,d}(t)$ (recursive polynomials of degree d) controlling the curve shape.

Due to the ambiguity of curves using 3D B-Splines (the same spline curve can be described by different configurations of its control points), regressing all three dimensions per control point results in strong overfitting during training. We resolve this issue by limiting the degrees of freedom per control point to two and constraining the control points deflection to one direction in the x-y-plane and one direction in the y-z-plane as illustrated in Fig. 2. More precisely, the degrees of freedom per control point are specified by the directions of the normals $\mathbf{N}_{xy}$ and N_z of an initial curve proposal $\bar{\boldsymbol{f}}$ with control points $\bar{\boldsymbol{c}}_k = \left(\bar{x}_k, \bar{y}_k, \bar{z}_k \right)^T$. The control points are then defined as

$$\boldsymbol{c}_k = \begin{pmatrix} x_k \\ y_k \\ z_k \end{pmatrix} = \begin{pmatrix} \bar{x}_k + \mathrm{N}_x \cdot \alpha_k \\ \bar{y}_k + \mathrm{N}_y \cdot \alpha_k \\ \bar{z}_k + \mathrm{N}_z \cdot \beta_k \end{pmatrix}, \qquad (2)$$

where N_x, N_y describe the x- and y-component of the normal vector $\mathbf{N}_{xy}$ in the x-y-plane. As shown in Eq. (2) and illustrated in Fig. 2, modeling splines as deflections in normal direction of its underlying initial line proposal only requires two parameters α_k, β_k per control point to describe the 3D shape. We use a wide variety of orientations for the initial proposals $\bar{\boldsymbol{f}}$ (see Fig. 2), which allows us to detect any kind of lines with this formulation. More details about the initial proposals are provided in the supplementary.

While [32] models the curve range using start- and end-points that are learned by means of regression, we instead propose to model visibility[1] using a continuous representation $v(t)$ and treat the visibility estimation as a classification problem. We obtain probability values applying sigmoid activation and consider $\sigma\big(v(t)\big) > 0.5$ the visible range. While in theory any kind of function can be utilized, we found that B-Splines with the same configuration as $\boldsymbol{f}(t)$ are well-suited and introduce spline control points γ_k defining the shape of $v(t)$.

Eventually, binary cross-entropy is used as a classification loss to learn visibility

$$\mathcal{L}_{vis} = -\frac{1}{|\mathcal{P}_{GT}|} \sum_{\boldsymbol{p} \in \mathcal{P}_{GT}} \hat{v}_{\boldsymbol{p}} \cdot \log\big(\sigma\big(v(t_{\boldsymbol{p}})\big)\big) + \qquad (3)$$

$$(1 - \hat{v}_{\boldsymbol{p}}) \cdot \log\big(1 - \sigma\big(v(t_{\boldsymbol{p}})\big)\big), \qquad (4)$$

---

[1]For the concept of visibility, we follow the prevailing definition from the literature [2, 9].
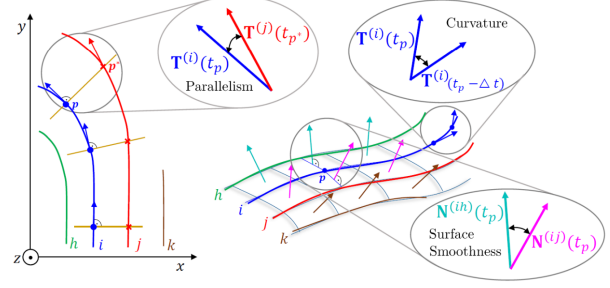

Figure 3. Illustration of different priors expressed by line tangents and surface normals.

where $\mathcal{P}_{GT}$ denotes the ground truth set of points, $\hat{v}_{\boldsymbol{p}} \in \{0, 1\}$ the ground truth visibility for point $\boldsymbol{p}$. $t_{\boldsymbol{p}}$ represents the respective curve argument obtained by orthogonal projection of $\boldsymbol{p}$ onto the underlying line proposal.

3.2. Regularization using physical priors

In this section, we describe our regularization method to integrate prior knowledge about lane structure and surface geometry into our parametric line representation (see Fig. 3).

Line parallelism. In order to reinforce parallel lines, the tangents at point pairs located in opposite normal direction on neighboring lines must be similar (see Fig. 3 left). We realize this by penalizing the cosine distance of the unit tangents $\mathbf{T}(t)$ on neighboring lines i and j for normal point pairs. More precisely, for each point $\boldsymbol{p} \in \mathcal{P}^{(i)}$ on line i we select the normal pair point $\boldsymbol{p}^*$ on neighbor line j that minimizes the distance to the normal plane, which is defined by the plane equation $\mathbf{T}^{(i)}(t)^T \cdot \big((x,y,z)^T - \boldsymbol{f}^{(i)}(t)\big) = 0$. In Fig. 3 the normal planes are visualized in a 2D top-view as lines (orange) for simplicity. Hence the respective curve argument $t_{\boldsymbol{p}^*}$ for point $\boldsymbol{p}^*$ on line j is given as

$$t_{\boldsymbol{p}^*} = \operatorname*{argmin}_{\boldsymbol{p}' \in \mathcal{P}^{(j)}} \mathbf{T}^{(i)}(t_{\boldsymbol{p}})^T \cdot \big(\boldsymbol{f}^{(j)}(t_{\boldsymbol{p}'}) - \boldsymbol{f}^{(i)}(t_{\boldsymbol{p}})\big), \quad (5)$$

where $\mathcal{P}^{(j)}$ denotes the points on line j. While in theory Eq. (5) can be solved analytically, the simpler way is to sample the set of points $\mathcal{P}^{(j)}$ instead. (Note that our continuous representation allows us to choose high sampling rates without losing precision as no interpolation is required.)

With the normal point pairs, we define the parallelism loss for a neighbor line pair based on the cosine distance of their tangents as

$$\mathcal{L}_{par}^{(ij)} = \frac{\mathbb{1}_{\boldsymbol{p}}^{(ij)}}{|\mathcal{P}^{(i)}|} \cdot \sum_{\boldsymbol{p} \in \mathcal{P}^{(i)}} 1 - \big(\mathbf{T}^{(i)}(t_{\boldsymbol{p}})\big)^T \cdot \mathbf{T}^{(j)}(t_{\boldsymbol{p}^*}). \quad (6)$$

Since the criterion of line parallelism should not hold for all normal point pairs of neighboring lines (e.g. merging or splitting lines), $\mathbb{1}_{\boldsymbol{p}}^{(ij)} \in \{0, 1\}$ represents the indicator

function determining whether the parallelism loss is applied to the point pair. More precisely, the function ensures that only the overlapping range of neighboring lines is taken into account. Furthermore, it determines whether the line pair should be considered as a parallel pair based on the standard deviation of euclidean distances between normal point pairs, i.e. high deviations indicate that the line pair might belong to a merge or split structure. In our experiments, we achieve state-of-the-art performance on test sets containing merges and splits, proving that our model is also capable of learning non-parallel line pairs using this indicator function.

Surface smoothness. Since the lines reside on a smooth road, the surface normals of neighboring lanes should be similar. Analogously to $\mathcal{L}_{par}$, we express this with the cosine distance between surface normals $\mathbf{N}^{(ih)}$ and $\mathbf{N}^{(ij)}$ as

$$\mathcal{L}_{sm}^{(i)} = \frac{\mathbb{1}_{\boldsymbol{p}}^{(hij)}}{|\mathcal{P}^{(i)}|} \cdot \sum_{\boldsymbol{p} \in \mathcal{P}^{(i)}} 1 - \left(\mathbf{N}^{(ih)}(t_{\boldsymbol{p}})\right)^T \cdot \mathbf{N}^{(ij)}(t_{\boldsymbol{p}}), \quad (7)$$

with indicator function $\mathbb{1}_{\boldsymbol{p}}^{(hij)}$. The surface normal between line i and left neighbor line h at point $\boldsymbol{p}$ can be expressed as the cross product of the tangent on line i and the normalized connection vector between lines i and h, hence $\mathbf{N}^{(ih)}(t_{\boldsymbol{p}}) = \mathbf{T}^{(i)}(t_{\boldsymbol{p}}) \times \frac{\boldsymbol{f}^{(h)}(t_{\boldsymbol{p}^*}) - \boldsymbol{f}^{(i)}(t_{\boldsymbol{p}})}{||\boldsymbol{f}^{(h)}(t_{\boldsymbol{p}^*}) - \boldsymbol{f}^{(i)}(t_{\boldsymbol{p}})||}$. For the normal between line i and right neighbor j the sign is flipped to obtain upwards pointing normal vectors.

Curvature. We determine lane curvature by computing the second order derivatives as the difference of tangents at consecutive points divided by their euclidean distance as $\mathbf{T}'(t_{\boldsymbol{p}}) = \frac{\mathbf{T}(t_{\boldsymbol{p}}) - \mathbf{T}(t_{\boldsymbol{p}} - \Delta t)}{||\boldsymbol{f}(t_{\boldsymbol{p}}) - \boldsymbol{f}(t_{\boldsymbol{p}} - \Delta t)||}$. The maximum curvature in x-y-plane (inverse curve radius) and in z (rate of slope change) have very different value ranges and are therefore restricted by different limits. Hence, we define the two thresholds κ_{xy} and κ_z and formulate the curvature loss on line i as

$$\mathcal{L}_{curv}^{(i)} = \frac{1}{|\mathcal{P}^{(i)}|} \cdot \sum_{\boldsymbol{p} \in \mathcal{P}^{(i)}} \max\left(\mathrm{T}_{xy}'^{(i)}(t_{\boldsymbol{p}}), \kappa_{xy}\right) \quad (8)$$

$$+ \max\left(\mathrm{T}_z'^{(i)}(t_{\boldsymbol{p}}), \kappa_z\right). \quad (9)$$

Finally, the prior regularization loss is given as

$$\mathcal{L}_{prior} = \sum_{i=1}^{M} \lambda_{sm} \mathcal{L}_{sm}^{(i)} + \lambda_{curv} \mathcal{L}_{curv}^{(i)} + \sum_{j=1}^{N} \lambda_{par} \mathcal{L}_{par}^{(ij)}, \quad (10)$$

with individual weights $\lambda_{par}, \lambda_{sm}, \lambda_{curv}$. Note that all these properties are expressible by means of tangents and normals, which can be computed analytically on our parametric representation in continuous space. Consequently, minimization of the herein introduced prior losses does not depend on numerical approximations as is the case for anchor-, grid- or key-point representations.
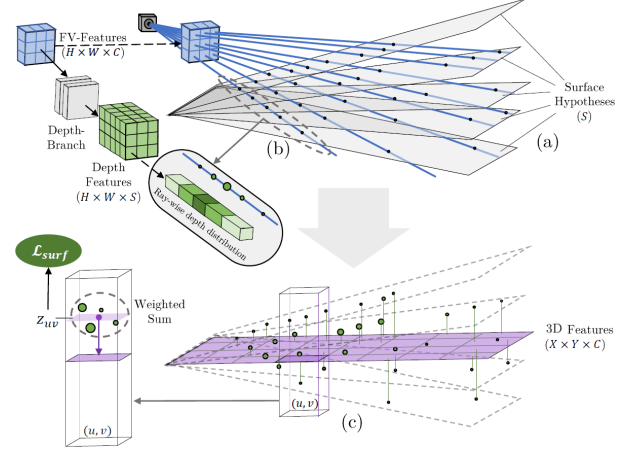

Figure 4. Our proposed spatial transformation module. First, several road surface hypotheses are defined (a) to which front-view features are lifted (b) and weighted according to the predicted depth distribution. Afterwards, point features are aggregated in a weighted manner to obtain the 3D feature map (c).

3.3. Spatial transformation

In this section, we describe our spatial transformation (shown in Fig. 4) that is leveraging valuable physical knowledge about surface geometry. We know that the road surface typically shows small deviations from the ground level ($z = 0$) in the near-range and stronger deviations in the far-range. Based on this knowledge, we sample ground surface hypotheses that reflect the distribution of the road surface height profile (Fig. 4a). While in theory different types of surface functions could be utilized as hypotheses, we decide to merely rely on planes, since this facilitates the computation of ray intersections described in the following step.

Next, the multi-scale front-view feature maps extracted by the backbone are lifted to 3D space (Fig. 4b). Our approach is inspired by [31], where front-view features are spreading along rays throughout the space of the road surface. These rays intersect with the surface hypotheses at different depths spanning a frustum-like point cloud in 3D space, where each point is affiliated with a C-dimensional feature vector and additionally attached with its height value z, hence, each point in the cloud has dimension $(C + 1)$. The front-view feature map is propagated through a depth branch with a channel-wise softmax applied to obtain a categorical distribution for each ray, resulting in a tensor of size $H \times W \times S$, where H, W denote height and width and channel size S the number of surface hypotheses.

In order to aggregate the information in 3D space, a BEV grid of size $X \times Y$ is defined. Features from points mapping to the same grid cell are weighted by the categorical depth distribution for the respective ray and accumulated in terms of a weighted sum (Fig. 4c). Since the z-component

Priors	F1(%)↑	X-near(m)↓	X-far(m)↓	Z-near(m)↓	Z-far(m)↓
None	65.0	0.316	0.384	0.106	0.153
Par.	66.2	0.291	0.373	0.103	0.150
Surf.	65.8	0.320	0.356	0.103	0.144
Curv.	66.7	0.322	0.366	0.105	0.146
Comb.	66.7	0.301	0.359	0.103	0.144

Table 1. Effect of different prior losses on OpenLane300.

# Surface Hypotheses	1	3	5	15	27
F1-Score(%)↑	65.0	65.9	**66.6**	66.1	66.0

Table 2. Effect of the surface hypotheses on OpenLane300.

Lane Rep.	Prior Reg.	Spatial T.	F1(%)↑	Gain(%)
			62.9	(baseline)
✓			65.0	+2.1
✓	✓		66.7	+3.8
✓		✓	66.6	+3.7
✓	✓	✓	**66.9**	**+4.0**

Table 3. Performance gain for different contributions on Open-Lane300 using our novel **Lane Representation**, **Prior Regularization** and **Spatial Transformation** instead of IPM.

of the points is also combined by a weighted sum, the value z_{uv} can be interpreted as the height value of the surface for grid cell (u, v). We guide the model in learning the real surface and prevent it from learning an arbitrary mapping by introducing a simple grid-based regression loss as

$$\mathcal{L}_{surf} = \frac{1}{X \cdot Y} \sum_{(u,v) \in X \times Y} \mathbb{1}_{uv} \cdot \|z_{uv} - \hat{z}_{uv}\|_1, \quad (11)$$

with $\mathbb{1}_{uv}$ indicating whether surface ground truth $\hat{z}_{uv}$ is available for cell (u, v). The height ground truth is obtained by interpolation of the 3D lane annotations at cell locations.

3.4. Loss functions

The overall loss used during training is given as the weighted sum of loss components

$$\mathcal{L} = \lambda_{pr}\mathcal{L}_{pr} + \lambda_{cat}\mathcal{L}_{cat} + \lambda_{reg}\mathcal{L}_{reg} + \quad (12)$$
$$\lambda_{vis}\mathcal{L}_{vis} + \lambda_{prior}\mathcal{L}_{prior} + \lambda_{surf}\mathcal{L}_{surf}. \quad (13)$$

We use focal loss [21] for lane presence $\mathcal{L}_{pr}$ and category classification $\mathcal{L}_{cat}$. For the regression loss $\mathcal{L}_{reg}$, we adapt the formulation of [32] to three instead of two dimensions. More details are provided in the supplementary.

4. Experiments

We first describe our experimental setup and then analyze our approach on two 3D lane datasets.
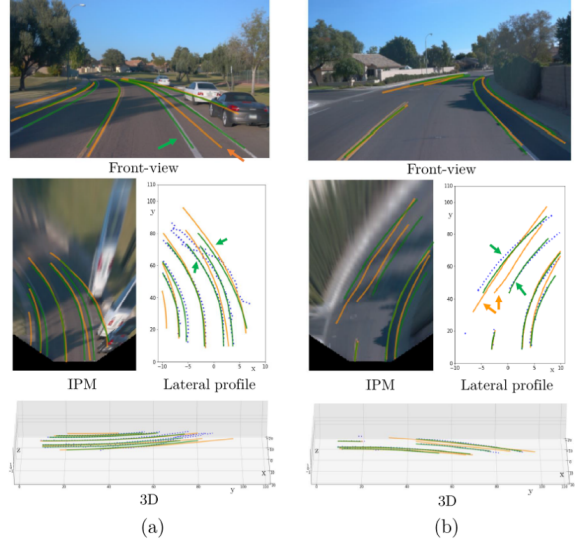

Figure 5. Qualitative comparison of our model trained with prior regularization to the same model without regularization both trained on OpenLane300 with main differences highlighted by arrows. As a reference ground truth lines are visualized dashed.

4.1. Experimental setup

We evaluate our method on two different datasets: Open-Lane and Apollo 3D Synthetic - both containing 3D lane ground truth as well as camera parameters per frame.

OpenLane [2] is a real-world dataset containing 150,000 images in the training and 40,000 in the test set from 1000 different sequences. In order to evaluate different driving scenarios the test set is divided into different situations, namely *Up & Down*, *Curve*, *Extreme Weather*, *Night*, *Intersection* and *Merge & Split*. For ablation studies we use the smaller version OpenLane300 including 300 sequences.

Apollo 3D Synthetic [9] is a small synthetic dataset, consisting of only 10,500 examples from rather simple scenarios of highway, urban and rural environments. The data is split into three subsets, *(1) Standard* (simple) scenarios, *(2) Rare Scenes* and *(3) Visual Variations*.

Evaluation metrics. For the quantitative evaluation both datasets utilize the evaluation scheme proposed in [9]. It evaluates the euclidean distance at uniformly distributed points in the range of 0-100 m along the y-direction. Based on the mean distance and range, *F1-Score* is computed, as well as the mean x- and z-errors in *near-* (0-40 m) and *far-range* (40-100 m) to evaluate geometric accuracy.

Baseline. Our approach builds up on 3D-SpLineNet. Since it was applied on synthetic data only, it showed poor performance on real data. We applied some straight-forward design adaptations - e.g. larger backbone, multi-scale features (see supplementary) - and use this modified 3D-SpLineNet as our baseline (first row Table 3).

| Method | F1-Score(%)↑ | X-error near(m)↓ | X-error far(m)↓ | Z-error near(m)↓ | Z-error far(m)↓ | F1-Score(%) per Scenario ↑ | | | | | |
						U&D	C	EW	N	I	M&S
3D-LaneNet [6]	44.1	0.479	0.572	0.367	0.443	40.8	46.5	47.5	41.5	32.1	41.7
Gen-LaneNet [9]	32.3	0.591	0.684	0.411	0.521	25.4	33.5	28.1	18.7	21.4	31.0
PersFormer [2]	50.5	0.485	0.553	0.364	0.431	42.4	55.6	48.6	46.6	40.0	50.7
PersFormer* [2]	53.1	0.361	0.328	0.124	<u>0.129</u>	46.8	58.7	<u>54.0</u>	48.4	41.4	52.5
CurveFormer [1]	50.5	0.340	0.772	0.207	0.651	45.2	56.6	49.7	49.1	42.9	45.4
BEV-LaneDet [46]	<u>58.4</u>	0.309	0.659	0.244	0.631	<u>48.7</u>	<u>63.1</u>	53.4	<u>53.4</u>	<u>50.3</u>	<u>53.7</u>
Anchor3DLane [12]	53.7	0.276	<u>0.311</u>	0.107	0.138	46.7	57.2	52.5	47.8	45.4	51.2
Anchor3DLane-T [12]	54.3	<u>0.275</u>	**0.310**	<u>0.105</u>	0.135	47.2	58.0	52.7	48.7	45.8	51.7
LaneCPP (Ours)	**60.3**	**0.264**	**0.310**	**0.077**	**0.117**	**53.6**	**64.4**	**56.7**	**54.9**	**52.0**	**58.7**

Table 4. Quantitative comparison on OpenLane [2]. **Best performance** and <u>second best</u> are highlighted. The scenario categories are Up and Down (U&D), Curve (C), Extreme Weather (EW), Night (N), Intersection (I), Merge and Split (M&S). PersFormer* denotes the latest performance reported on the official code base, Anchor3DLane-T represents the temporal multi-frame method of [12].
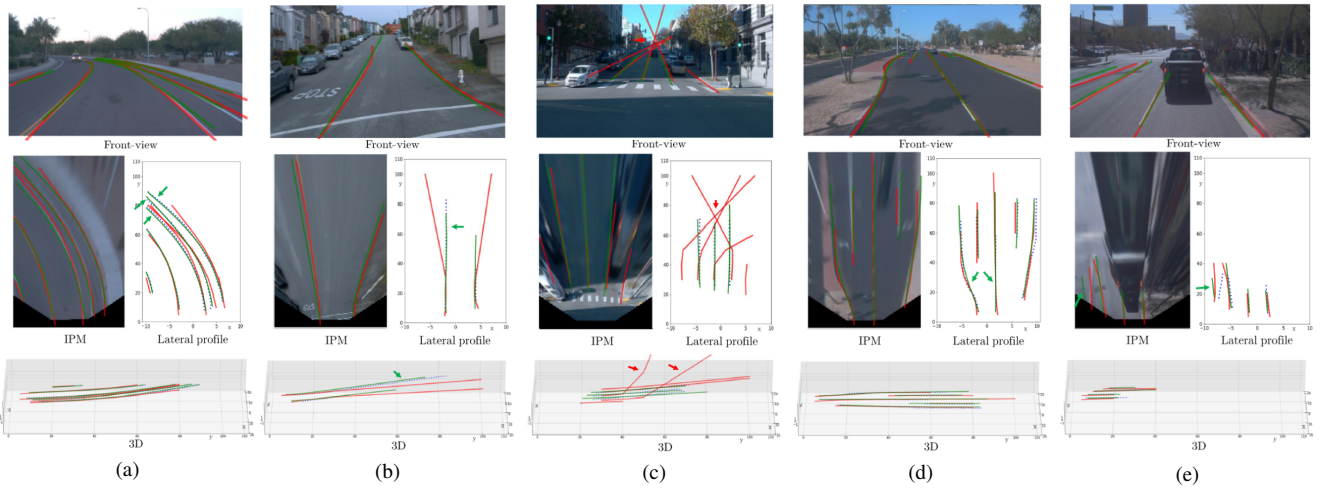

Figure 6. Qualitative comparison on OpenLane. Our method is compared to PersFormer* with ground truth visualized as dashed lines.

Implementation details. We use input size 360×480 and adopt the same backbone as in [2] based on a modified EfficientNet [42]. We extract four feature maps of resolutions $[\frac{1}{2}, \frac{1}{4}, \frac{1}{8}, \frac{1}{16}]$. The final 3D feature map has size 26×16 with 64 channels. We use $M = 64$ initial line proposals and B-Splines of degree $d = 3$ and $K = 10$ control points. We apply Adam optimizer [14] with an initial learning rate of 2×10^{-4} for OpenLane and 10^{-4} for Apollo and a dataset specific step-wise scheduler. We train for 30 epochs on OpenLane and 300 epochs on Apollo with batch size 16. For more details we refer to the supplementary.

4.2. Ablation studies

Table 1 indicates the effect of our proposed prior-based regularization. It is evident that each prior improves the F1-Score as well as geometric errors. While the surface and curvature priors result in better far-range estimates, line parallelism supports X-regression in the near-range. Besides, using surface smoothness loss results in lowest Z-far errors. Finally, a combination of priors yields a good balance of

F1-Score and geometric errors. The positive effect of parallelism is confirmed by Fig. 5, where reinforcing parallel lane structure leads to better estimates in the near-range (a) and far-range (b) compared to the unregularized model. Learning parallel lines also is evidently beneficial in cases of poor visibility (b) and occlusions (a). In the latter case, the regularized model even shows better predictions than the noisy ground truth. This emphasizes the high relevance of priors for more robust behavior for real-world datasets, where 3D ground truth often comes with inaccuracies.

For the spatial transformation (see Table 2), too low numbers of surface hypotheses result in worse score, presumably as 3D geometry is not captured sufficiently, whereas larger numbers tend to decreasing performance due to the higher complexity. The best F1-Score is obtained with 5 hypotheses, which is chosen for further experiments. While the improvement over IPM is already considerable, we think that with the simplifications of plane hypotheses prevent the component from developing its full potential. We see ways to enhance the 3D transformation even further

Method	Balanced Scenes					Rare Scenes				
	F1(%)↑	X-error (m) ↓		Z-error (m) ↓		F1(%)↑	X-error (m) ↓		Z-error (m) ↓	
		near	far	near	far		near	far	near	far
3D-LaneNet [6]	86.4	0.068	0.477	0.015	**0.202**	72.0	0.166	0.855	0.039	**0.521**
GP [17]	91.9	0.049	0.387	**0.008**	0.213	83.7	0.126	0.903	<u>0.023</u>	0.625
PersFormer [2]	92.9	0.054	0.356	0.01	0.234	87.5	0.107	0.782	0.024	0.602
3D-SpLineNet [32]	96.3	0.037	0.324	<u>0.009</u>	0.213	92.9	0.077	0.699	**0.021**	0.562
CurveFormer [1]	95.8	0.078	0.326	0.018	0.219	95.6	0.182	0.737	0.039	0.561
BEV-LaneDet [46]	96.9	**0.016**	**0.242**	0.02	0.216	**97.6**	**0.031**	**0.594**	0.040	0.556
Anchor3DLane [12]	95.4	0.045	0.300	0.016	0.223	94.4	0.082	0.699	0.030	0.580
LaneCPP (Ours)	**97.4**	<u>0.030</u>	<u>0.277</u>	0.011	<u>0.206</u>	<u>96.2</u>	<u>0.073</u>	<u>0.651</u>	<u>0.023</u>	<u>0.543</u>

Table 5. Quantitative comparison of best methods on Apollo 3D Synthetic [9]. **Best performance** and <u>second best</u> are highlighted.

using more sophisticated spatial representations in future.

The impact of our different contributions is summarized in Table 3, where the first row shows our baseline (see Sec. 4.1). More than two percent in F1-Score are gained with our novel lane representation compared to the simplified one from [32]. Moreover, it is clear that both, the regularization using combined priors and the spatial transformation using 5 hypotheses result in significant improvement. Eventually, combining all components yields the best model configuration, which we choose for further evaluation.

4.3. Evaluation on OpenLane

On the real-world OpenLane benchmark our model evidently outperforms all other methods with respect to F1-Score as well as geometric errors as shown in Table 4. Compared to BEV-Lanedet, which achieves a high detection score, our model gains +1.9%, while reaching significantly lower geometric errors. In comparison to Anchor3DLane the improvements with respect to X-errors are less substantial, however, our approach surpasses the F1-Score by a large gap of +6.6%. Analyzing the detection scores among different scenarios, outstanding performance gain is observed on the up- and down-hill test set (+5.9%) that highlights the capability of our approach to capture 3D space proficiently, which is supported by the low Z-errors.

Apart from quantitative results, we show qualitative examples in Fig. 6. In up-hill scenarios like Fig. 6b our model manages to estimate both lateral and height profile accurately, since our assumptions about road surface and line parallelism are satisfied. In contrast, PersFormer lacks spatial features and does not use any kind of physical regularization. Consequently, it fails to estimate the 3D lane geometry and even collapses in Fig. 6c, whereas our surface and curvature priors always prevent such a behavior. Noteworthy is also the top performance on the merges and splits set. This proves that our soft regularization is even capable to handle situations containing non-parallel lines, which is also confirmed by Fig. 6d. However, we rarely observe limi-

tations with our formulation for line pairs with a similar orientation but weakly converging course as shown in Fig. 6e. In such cases the indicator function might erroneously decide for parallelism loss during training. One possible solution for future work would be to consider ground truth for the indicator function to identify such situations.

4.4. Evaluation on Apollo 3D Synthetic

The Apollo 3D Synthetic dataset is very limited in size and only consists of simple situations in contrast to OpenLane. While we find the results on OpenLane more meaningful, we would like to still provide and discuss the quantitative results on the Apollo dataset. Due to the simplicity of the dataset, our model cannot benefit that significantly from our priors but still achieves competitive results to state of the art with the highest F1-Score on the balanced scenes dataset and comparable error metrics (second best for most errors).

5. Conclusions and future work

In this work, we present LaneCPP, a novel approach for 3D lane detection that leverages physical prior knowledge about lane structure and road geometry. Our new continuous lane representation overcomes previous deficiencies by allowing arbitrary lane structures and enables us to regularize lane geometry based on analytically formulated priors. We further introduce a novel spatial transformation module that models 3D features carefully considering knowledge about road surface geometry. In our experiments, we demonstrate state-of-the-art performance on real and synthetic benchmarks. The full capability of our approach is revealed on real-world OpenLane, for which we prove the relevance of priors quantitatively and qualitatively. In future, priors could be individualized for different driving scenarios and might support to learn inter-lane relations to achieve better scene understanding in a global context. We also see ways to leverage the full potential of the spatial transformation by using more sophisticated surface representations.

References

[1] Yifeng Bai, Zhirong Chen, Zhangjie Fu, Lang Peng, Peng-peng Liang, and Erkang Cheng. Curveformer: 3d lane detection by curve propagation with curve queries and attention. In *Proc. IEEE International Conf. on Robotics and Automation (ICRA)*, 2023. 1, 2, 3, 7, 8

[2] Li Chen, Chonghao Sima, Yang Li, Zehan Zheng, Jiajie Xu, Xiangwei Geng, Hongyang Li, Conghui He, Jianping Shi, Yu Qiao, et al. Persformer: 3d lane detection via perspective transformer and the openlane benchmark. In *Proc. of the European Conf. on Computer Vision (ECCV)*, 2022. 2, 3, 4, 6, 7, 8

[3] Carl de Boor. On calculating with b-splines. *Journal of Approximation Theory*, 1972. 2

[4] Netalee Efrat, Max Bluvstein, Shaul Oron, Dan Levi, Noa Garnett, and Bat El Shlomo. 3d-lanenet+: Anchor free lane detection using a semi-local representation. *arXiv/2011.01535*, 2020. 1, 2, 3

[5] Zhengyang Feng, Shaohua Guo, Xin Tan, Ke Xu, Min Wang, and Lizhuang Ma. Rethinking efficient lane detection via curve modeling. In *Proc. IEEE Conf. on Computer Vision and Pattern Recognition (CVPR)*, 2022. 2

[6] Noa Garnett, Rafi Cohen, Tomer Pe'er, Roee Lahav, and Dan Levi. 3d-lanenet: End-to-end 3d multiple lane detection. In *Proc. of the IEEE International Conf. on Computer Vision (ICCV)*, 2019. 1, 2, 3, 7, 8

[7] Mohsen Ghafoorian, Cedric Nugteren, Nóra Baka, Olaf Booij, and Michael Hofmann. EL-GAN: embedding loss driven generative adversarial networks for lane detection. In *Proc. of the European Conf. on Computer Vision (ECCV)*, 2018. 1, 2

[8] Stephen Gould, Richard Hartley, and Dylan Campbell. Deep declarative networks. *IEEE Trans. on Pattern Analysis and Machine Intelligence (PAMI)*, 2021. 2

[9] Yuliang Guo, Guang Chen, Peitao Zhao, Weide Zhang, Jinghao Miao, Jingao Wang, and Tae Eun Choe. Gen-lanenet: A generalized and scalable approach for 3d lane detection. In *Proc. of the European Conf. on Computer Vision (ECCV)*, 2020. 1, 2, 3, 4, 6, 7, 8

[10] Steffen Hagedorn, Marcel Milich, and Alexandru P. Condurache. Pioneering se (2)-equivariant trajectory planning for automated driving. *arXiv:2403.11304*, 2024. 2

[11] Yuenan Hou, Zheng Ma, Chunxiao Liu, and Chen Change Loy. Learning lightweight lane detection cnns by self attention distillation. In *Proc. of the IEEE International Conf. on Computer Vision (ICCV)*, 2019. 1, 2

[12] Shaofei Huang, Zhenwei Shen, Zehao Huang, Zi han Ding, Jiao Dai, Jizhong Han, Naiyan Wang, and Si Liu. Anchor3dlane: Learning to regress 3d anchors for monocular 3d lane detection. In *Proc. IEEE Conf. on Computer Vision and Pattern Recognition (CVPR)*, 2023. 2, 3, 7, 8

[13] Brody Huval, Tao Wang, Sameep Tandon, Jeff Kiske, Will Song, Joel Pazhayampallil, Mykhaylo Andriluka, Pranav Rajpurkar, Toki Migimatsu, Royce Cheng-Yue, Fernando A. Mujica, Adam Coates, and Andrew Y. Ng. An empirical evaluation of deep learning on highway driving. *arXiv/1504.01716*, 2015. 1, 2

[14] Diederik P. Kingma and Jimmy Ba. Adam: A method for stochastic optimization. In *Proc. of the International Conf. on Learning Representations (ICLR)*, 2015. 7

[15] YeongMin Ko, Jiwon Jun, Donghwuy Ko, and Moongu Jeon. Key points estimation and point instance segmentation approach for lane detection. *arXiv/2002.06604*, 2020. 1, 2

[16] Seokju Lee, Junsik Kim, Jae Shin Yoon, Seunghak Shin, Oleksandr Bailo, Namil Kim, Tae-Hee Lee, Hyun Seok Hong, Seung-Hoon Han, and In So Kweon. Vpgnet: Vanishing point guided network for lane and road marking detection and recognition. In *Proc. of the IEEE International Conf. on Computer Vision (ICCV)*, 2017. 1, 2

[17] Chenguang Li, Jia Shi, Ya Wang, and Guangliang Cheng. Reconstruct from top view: A 3d lane detection approach based on geometry structure prior. In *Proc. IEEE Conf. on Computer Vision and Pattern Recognition (CVPR)*, 2022. 2, 3, 8

[18] Qi Li, Yue Wang, Yilun Wang, and Hang Zhao. Hdmapnet: An online HD map construction and evaluation framework. In *Proc. IEEE International Conf. on Robotics and Automation (ICRA)*, 2022. 3

[19] Xiang Li, Jun Li, Xiaolin Hu, and Jian Yang. Line-cnn: End-to-end traffic line detection with line proposal unit. *IEEE Trans. on Intelligent Transportation Systems (T-ITS)*, 2020. 1, 2

[20] Zhiqi Li, Wenhai Wang, Hongyang Li, Enze Xie, Chonghao Sima, Tong Lu, Yu Qiao, and Jifeng Dai. Bevformer: Learning bird's-eye-view representation from multi-camera images via spatiotemporal transformers. In *Proc. of the European Conf. on Computer Vision (ECCV)*, 2022. 3

[21] Tsung-Yi Lin, Priya Goyal, Ross B. Girshick, Kaiming He, and Piotr Dollár. Focal loss for dense object detection. In *Proc. of the IEEE International Conf. on Computer Vision (ICCV)*, 2017. 6

[22] Ruijin Liu, Zejian Yuan, Tie Liu, and Zhiliang Xiong. End-to-end lane shape prediction with transformers. In *Proc. of the IEEE Winter Conference on Applications of Computer Vision (WACV)*, 2021. 2

[23] Ruijin Liu, Dapeng Chen, Tie Liu, Zhiliang Xiong, and Zejian Yuan. Learning to predict 3d lane shape and camera pose from a single image via geometry constraints. In *Proc. of the Conf. on Artificial Intelligence (AAAI)*, 2022. 1, 2, 3

[24] Pingping Lu, Chen Cui, Shaobing Xu, Huei Peng, and Fan Wang. SUPER: A novel lane detection system. *IEEE Trans. on Intelligent Vehicles (T-IV)*, 2021. 2

[25] Hanspeter Mallot, Heinrich Blthoff, J.J. Little, and S Bohrer. Inverse perspective mapping simplifies optical flow computation and obstacle detection. *Biological Cybernetics*, 1991. 3

[26] Davy Neven, Bert De Brabandere, Stamatios Georgoulis, Marc Proesmans, and Luc Van Gool. Towards end-to-end lane detection: an instance segmentation approach. In *Proc. IEEE Intelligent Vehicles Symposium (IV)*, 2018. 1, 2

[27] Marcos Nieto, Luis Salgado, Fernando Jaureguizar, and Jon Arróspide. Robust multiple lane road modeling based on perspective analysis. In *Proc. IEEE International Conf. on Image Processing (ICIP)*, 2008. 2

[28] Bowen Pan, Jiankai Sun, Ho Yin Tiga Leung, Alex Andonian, and Bolei Zhou. Cross-view semantic segmentation for sensing surroundings. *IEEE Robotics Autom. Lett.*, 2020. 3

[29] Xingang Pan, Jianping Shi, Ping Luo, Xiaogang Wang, and Xiaoou Tang. Spatial as deep: Spatial CNN for traffic scene understanding. In *Proc. of the Conf. on Artificial Intelligence (AAAI)*, 2018. 1, 2

[30] Lang Peng, Zhirong Chen, Zhangjie Fu, Pengpeng Liang, and Erkang Cheng. Bevsegformer: Bird's eye view semantic segmentation from arbitrary camera rigs. In *Proc. of the IEEE Winter Conference on Applications of Computer Vision (WACV)*, 2023. 3

[31] Jonah Philion and Sanja Fidler. Lift, splat, shoot: Encoding images from arbitrary camera rigs by implicitly unprojecting to 3d. In *Proc. of the European Conf. on Computer Vision (ECCV)*, 2020. 3, 5

[32] Maximilian Pittner, Alexandru Condurache, and Joel Janai. 3d-splinenet: 3d traffic line detection using parametric spline representations. In *Proc. of the IEEE Winter Conference on Applications of Computer Vision (WACV)*, 2023. 1, 2, 3, 4, 6, 8

[33] Fabio Pizzati, Marco Allodi, Alejandro Barrera, and Fernando García. Lane detection and classification using cascaded cnns. In *Proc. of the International Conf. on Computer Aided Systems Theory (EUROCAST)*, 2019. 1, 2

[34] Zhan Qu, Huan Jin, Yang Zhou, Zhen Yang, and Wei Zhang. Focus on local: Detecting lane marker from bottom up via key point. In *Proc. IEEE Conf. on Computer Vision and Pattern Recognition (CVPR)*, 2021. 1, 2

[35] Matthias Rath and Alexandru Paul Condurache. Invariant integration in deep convolutional feature space. In *Proc. of European Symposium on Artificial Neural Networks, Computational Intelligence and Machine Learning (ESANN)*, 2020. 2

[36] Matthias Rath and Alexandru Paul Condurache. Improving the sample-complexity of deep classification networks with invariant integration. In *Proc. of International Joint Conf. on Computer Vision, Imaging and Computer Graphics Theory and Applications (VISIGRAPP)*, 2022. 2

[37] Thomas Roddick and Roberto Cipolla. Predicting semantic map representations from images using pyramid occupancy networks. In *Proc. IEEE Conf. on Computer Vision and Pattern Recognition (CVPR)*, 2020. 3

[38] Thomas Roddick, Alex Kendall, and Roberto Cipolla. Orthographic feature transform for monocular 3d object detection. In *Proc. of the British Machine Vision Conf. (BMVC)*, 2019. 3

[39] Avishkar Saha, Oscar Mendez, Chris Russell, and Richard Bowden. Translating images into maps. In *Proc. IEEE International Conf. on Robotics and Automation (ICRA)*, 2022. 3

[40] Jinming Su, Chao Chen, Ke Zhang, Junfeng Luo, Xiaoming Wei, and Xiaolin Wei. Structure guided lane detection. In *Proc. of the International Joint Conf. on Artificial Intelligence (IJCAI)*, 2021. 2

[41] Lucas Tabelini, Rodrigo Berriel, Thiago M Paixao, Claudine Badue, Alberto F De Souza, and Thiago Oliveira-Santos. Keep your eyes on the lane: Real-time attention-guided lane detection. In *Proc. IEEE Conf. on Computer Vision and Pattern Recognition (CVPR)*, 2021. 1, 2

[42] Mingxing Tan and Quoc Le. Efficientnet: Rethinking model scaling for convolutional neural networks. In *Proc. of the International Conf. on Machine learning (ICML)*, 2019. 7

[43] Lucas Tabelini Torres, Rodrigo Ferreira Berriel, Thiago M. Paixão, Claudine Badue, Alberto F. De Souza, and Thiago Oliveira-Santos. Polylanenet: Lane estimation via deep polynomial regression. In *Proc. of the International Conf. on Pattern Recognition (ICPR)*, 2020. 2

[44] Bingke Wang, Zilei Wang, and Yixin Zhang. Polynomial regression network for variable-number lane detection. In *Proc. of the European Conf. on Computer Vision (ECCV)*, 2020. 2

[45] Jinsheng Wang, Yinchao Ma, Shaofei Huang, Tianrui Hui, Fei Wang, Chen Qian, and Tianzhu Zhang. A keypoint-based global association network for lane detection. In *Proc. IEEE Conf. on Computer Vision and Pattern Recognition (CVPR)*, 2022. 1, 2

[46] Ruihao Wang, Jian Qin, Kaiying Li, Yaochen Li, Dong Cao, and Jintao Xu. Bev-lanedet: An efficient 3d lane detection based on virtual camera via key-points. In *Proc. IEEE Conf. on Computer Vision and Pattern Recognition (CVPR)*, 2023. 2, 3, 7, 8

[47] Yuping Wang and Jier Chen. Eqdrive: Efficient equivariant motion forecasting with multi-modality for autonomous driving. *arXiv:2310.17540*, 2023. 2

[48] Lu Xiong, Zhenwen Deng, Peizhi Zhang, and Zhiqiang Fu. A 3d estimation of structural road surface based on lane-line information. *IFAC Conf. on Engine and Powertrain Control, Simulation and Modeling (E-COSM)*, 2018. 2

[49] Chenxin Xu, Robby T. Tan, Yuhong Tan, Siheng Chen, Yu Guang Wang, Xinchao Wang, and Yanfeng Wang. Eqmotion: Equivariant multi-agent motion prediction with invariant interaction reasoning. In *Proc. IEEE Conf. on Computer Vision and Pattern Recognition (CVPR)*, 2023. 2

[50] Fan Yan, Ming Nie, Xinyue Cai, Jianhua Han, Hang Xu, Zhen Yang, Chaoqiang Ye, Yanwei Fu, Michael Bi Mi, and Li Zhang. Once-3dlanes: Building monocular 3d lane detection. In *Proc. IEEE Conf. on Computer Vision and Pattern Recognition (CVPR)*, 2022. 2, 3

[51] Tu Zheng, Hao Fang, Yi Zhang, Wenjian Tang, Zheng Yang, Haifeng Liu, and Deng Cai. RESA: recurrent feature-shift aggregator for lane detection. In *Proc. of the Conf. on Artificial Intelligence (AAAI)*, 2021. 2

[52] Tu Zheng, Yifei Huang, Yang Liu, Wenjian Tang, Zheng Yang, Deng Cai, and Xiaofei He. Clrnet: Cross layer refinement network for lane detection. In *Proc. IEEE Conf. on Computer Vision and Pattern Recognition (CVPR)*, 2022. 2

[53] Qin Zou, Hanwen Jiang, Qiyu Dai, Yuanhao Yue, Long Chen, and Qian Wang. Robust lane detection from continuous driving scenes using deep neural networks. *IEEE Trans. on Vehicular Technology (VTC)*, 2020. 1, 2